ADVANCED SUSTAINABLE SYSTEMS
www.advsustainsys.com

Laser-Induced Graphene from Wood-Based Composites: Integrating Circuits in Bioderived Furniture

*Anna Chiara Bressi, Lucía Pérez Amaro, Benedetto Pizzo, Attilio Marino, Gianni Ciofani, and Francesco Greco**

The growing global demand for sustainability is driving the scientific community to explore alternative manufacturing approaches, particularly in the electronics field, where resource scarcity and e-waste pose significant environmental challenges. One promising solution is the direct patterning of laser-induced graphene (LIG) conductive tracks onto bioderived substrates. In this study, several wood panels are successfully fabricated with different resin formulations from *Jatropha curcas* L. seeds to reduce the urea-formaldehyde content, and the feasibility of LIG-based electronics on these panels is assessed. The panels' physical and mechanical properties are evaluated, including thickness swelling and internal bond strength, and conductive LIG is successfully scribed on all samples. Proofs of concept include a four-LED circuit and humidity sensors, with the best sensor achieving ≈0.2031 pF %RH^{-1} sensitivity and ≈5% hysteresis error. These results demonstrate the feasibility of embedding functional circuits into bioderived substrates and pave the way for sustainable smart furniture by integrating bioderived materials with advanced manufacturing techniques.

1. Introduction

Discovered in 2014,[1] Laser-Induced Graphene (LIG) has recently gained significant attention due to its exceptional properties, including high electrical and thermal conductivity[2] and large surface area.[3] LIG is synthesized through a laser scribing process, which converts carbon-rich precursors into 3D graphene-like structures via localized pyrolysis. This method stands out for its simplicity, scalability, and cost-effectiveness, as it employs commercially available infrared (IR) laser engravers and operates in ambient conditions without the need for chemicals or masks.[1] The resulting LIG can be directly patterned on various substrates and, if necessary, transferred onto other surfaces, making it highly suitable for applications in flexible electronics,[4] soft robotics,[5] energy storage,[6] physical[7,8] and electrochemical[9] sensing, surface wettability control,[10–12] and environmental remediation.[13,14]

The choice of precursor materials is crucial in determining the quality and performance of LIG. While synthetic polymeric LIG precursors initially caught the scientific community's interest,[1] the need for potentially more sustainable options has shifted the focus to their bioderived counterparts.[15–17] Among these, composite materials are interesting because their mechanical properties can be tuned to

A. C. Bressi, F. Greco
The Biorobotics Institute
Scuola Superiore Sant'Anna
Viale Rinaldo Piaggio 34, Pontedera 56025, Italy
E-mail: francesco.greco@santannapisa.it
A. C. Bressi, F. Greco
Department of Excellence in Robotics & AI
Scuola Superiore Sant'Anna
Piazza Martiri della Libertà 33, Pisa 56127, Italy
L. P. Amaro
Agroils Technologies Srl
Via Pietro Nenni 2, Sesto Fiorentino 50019, Italy
B. Pizzo
CNR-IBE
National Research Council of Italy
Institute of Bioeconomy
Via Madonna del Piano 10, Sesto Fiorentino 50019, Italy
A. Marino, G. Ciofani
Smart Bio-Interfaces
Istituto Italiano di Tecnologia
Viale Rinaldo Piaggio 34, Pontedera 56025, Italy
F. Greco
Interdisciplinary Center on Sustainability and Climate
Scuola Superiore Sant'Anna
Piazza Martiri della Libertà 33, Pisa 56127, Italy
F. Greco
Institute of Solid State Physics
NAWI Graz
Graz University of Technology
Petersgasse 16, Graz 8010, Austria

The ORCID identification number(s) for the author(s) of this article can be found under https://doi.org/10.1002/adsu.202500565

DOI: 10.1002/adsu.202500565

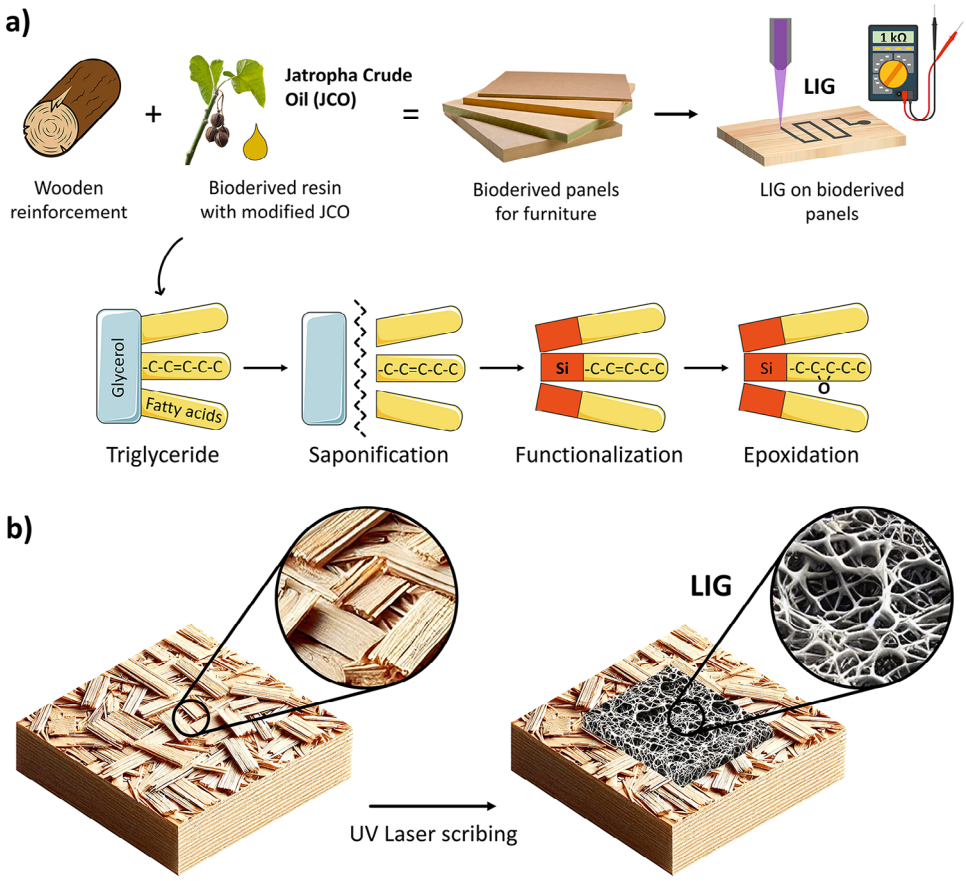

Figure 1. a) Schematic illustration of the composite manufacturing process, with an inset on JCO modification steps, and conductive LIG synthesis through laser-induced pyrolysis. b) Graphic illustration of the morphological change of the PB wood panel surface before and after laser scribing. For illustrative purposes only, the scale is adjusted for visual emphasis.

adapt to the specific application. In particular, wood-derived precursors and composites have been extensively studied as LIG precursors,[16,18–26] with satisfying results regarding sheet resistance and intensity ratios of Raman peaks. Effective LIG formation on these materials often requires thermal[19] and/or chemical pretreatment (e.g., fire-retardant coatings,[22,24,25] tannic acid/iron citrate inks[21] or lignin ink),[26] yielding low sheet resistance without damaging the substrate. Alternatively, scribing under inert atmospheres[20,22] or tailoring laser parameters can also be effective: defocused CO_2 beams,[18,19,24] more sophisticated femtosecond[21,27] and picosecond[23] lasers, or multistep scribing[24,25,27] have all been successfully employed. Similar strategies have also been adopted for other lignocellulosic materials, such as cork[28] and paper.[29] However, wood-based composites used in furniture are usually made with synthetic resins such as urea-formaldehyde (UF), melamine-urea-formaldehyde (MUF), phenol-formaldehyde (PF), and isocyanate compounds[30] (with a strong preference for UF),[31] due to their excellent adhesive properties and mechanical performance. These resins pose environmental and health concerns due to their petrochemical origin and the release of formaldehyde and other toxic chemicals.[32–34] Their use is being severely restricted due to their impact on human health and the environment.[35,36] As an alternative, the scientific community has focused on developing bioderived adhesives, which have demonstrated potential as cost-effective, environmentally sustainable, and health-conscious solutions.[35] Examples include adhesives made from lignin, tannins, proteins, natural rubber latex, carboxylic acids, and vegetable oils.[35,37]

In this study, we addressed these concerns by exploring, for the first time to the best of our knowledge, the potential of monounsaturated (MUFA) and polyunsaturated (PUFA) fatty acids from *Jatropha curcas* L. in bioderived matrices for wooden panel manufacturing, and the possibility of creating bioderived electronics on the finished products (**Figure 1a**).

In particular, *Jatropha curcas* L. crude oil (JCO) and seed kernels (JSK) are used to produce a bioderived adhesive compound. Jatropha is one of the 170 species belonging to the Euphorbiaceae family. It is a drought-resistant shrub or tree, widely distributed in the wild or semi-cultivated areas in Central and South America, Africa, and Southeast Asia. The JCO obtained from the plant seeds comprises different fatty acids, mostly MUFA and PUFA, the most abundant being oleic and linoleic acids, respectively.[38] JCO has several potential fields of applications: adhesives and resins[39,40] and biofuels[41–44] are the most important, while other less investigated uses are as fungicide,[45] antioxidant and antimicrobial agent,[46] lubricant,[47,48] and precursor for vegetable leather[49] or bio-polyurethanes.[50,39] JCO is cost-competitive with

Table 1. Distribution of virgin poplar wood chips particle size S.

	Poplar Wood Chips Size S distribution								
S [mm]	> 5	4–5	3–4	2–3	1–2	0.5–1	0.25–0.5	0.15–0.25	0–0.15
[%]	7.8	3.1	5.0	23.8	29.6	14.7	11.6	2.9	1.5

other commonly used oils such as soybean and rapeseed, making it an attractive option for wood adhesive applications in both industry and research.[51]

Here, the JCO is saponified to convert the triglycerides into free fatty acids, which are then chemically modified to improve their adhesive properties by reacting the acidic functional group at the end of the chain with silanes containing epoxides, and by direct in-chain epoxidation of the double bond in the MUFA and PUFA main chains. The chemically-modified JCO is added into a water-based biodispersion obtained from crushed JSK to form a bioderived compound, and the final resin is obtained by mixing the bioderived compound with the MUF in different percentages. The resin is then used to manufacture particle boards (PB), composite boards made from chips, under high pressure and temperature.[52,53] Virgin poplar and virgin hemp chips are used as bioderived lignocellulosic-based reinforcements.

Since wood-derived precursors and composites have been extensively studied as LIG precursors with satisfying results in terms of sheet resistance and Raman peak ratios,[16,18] the so-obtained panels are adopted as precursors to obtain conductive LIG patterns (Figure 1b). Two proof-of-concept of panels-embedded electronics are presented. The first is a circuit made of LIG tracks and four LEDs in series, to demonstrate the good conductivity of the graphene, while the second is an interdigitated humidity sensor, to investigate the possibility of sensorizing the substrate.

The approach presented here aims to balance functionality with sustainability thinking, reducing reliance on non-renewable resources and mitigating adverse health and environmental impacts, in alignment with the United Nations Sustainable Development Goals.

2. Experimental Section

2.1. Materials

Jatropha Crude Oil (JCO) and Jatropha Seed Kernel (JSK) were obtained from Jatropha seeds kindly supplied by Joil LTD – Singapore, the main owner of the world's biggest *Jatropha curcas* L. plantation located in Ghana, Africa. Oleic Acid (OA, technical grade 90%, CAS 112-80-1) and Linoleic Acid (LA, technical grade 54–78% with a minor content of Oleic Acid, CAS 60-33-3) were purchased from Sigma–Aldrich and used as reference MUFA and PUFA, respectively. (3-Glycidyloxypropyl)triethoxysilane (SIL, CAS 602-34-8) was purchased from Sigma–Aldrich and was used as an epoxide precursor.

Sodium hydroxide, hydrogen peroxide, hexane, glacial acetic acid, and ethanol were technical grade and used as received. Ion exchange resin Dowex 50WX2 was purchased from Sigma–Aldrich and used as a solid catalyst system. Melamine Urea – Formaldehyde resin (MUF) 11G300 and MUF 11H328, with 3% and 22% melamine content, respectively, were kindly supplied by ChemCom Industries – Netherlands.

Bio-dispersion with a 25% solid content of JSK was kindly supplied by Agroils Technologies – Italy. The virgin poplar wood chips were kindly provided by Invernizzi SpA – Italy and had a particle size distribution as reported in **Table 1**, while Hemp chips were kindly supplied by Rete Etruscum – Italy and had a particle size ≤ 2 mm.

Silver paste CI 1036 was purchased from Nagase ChemteX, and Polyimide sheets (Kapton thickness = 25.4 µm) from Dupont

2.2. Jatropha Crude Oil Chemical Modifications

JCO was mechanically extracted from *Jatropha curcas* L. seeds with a rotative cold press (COTER FRANCO series S205-80.f.s-2) at 80 RPM and 70 °C as set-point temperature. The extraction yield ranged from 25 to 30% in weight with respect to the initial biomass.

The functionalization of JCO followed three steps:

1) *Standard saponification*: During step 1, sodium hydroxide-catalyzed hydrolysis was exploited to separate triglycerides into glycerol and free fatty acids. The method was adapted from Salimon et al.[54] (substituting KOH with NaOH).
2) *End-chain functionalization with a silane precursor*: step 2 was carried out using a new synthetic route, exploiting the reactivity of silane groups toward carboxylate groups at the end of the fatty acid chains obtained after step 1 – saponification. The silane precursor included an epoxide group in its chemical structure.
3) *In-chain epoxidation*: step 3 consisted of the carbon double bonds in the chains being opened and epoxidized. Two methods for in-chain epoxidation were tried: Bhakri et al.[55] and Malarczyk-Matusiak et al.[56]

Fourteen oil samples were obtained starting from the pure oils (JCO, OA, LA) and by applying the aforementioned synthetic strategies. Although the three steps were consistently performed in the same sequence, not every step was applied to each sample. Their descriptions and codes are listed in **Table 2**.

Standard Saponification

Saponification (step 1) was only carried out on JCO. A 500 mL 3-neck round-bottom balloon equipped with a spiral refrigerator unit and temperature regulated by using a water bath and a magnetic heating plate was used as synthesis set-up. To saponify the JCO, 300 mL of ethanolic solution (90% v/v), 1.75 M of NaOH,

Table 2. Oil samples description and codes.

Code	Initial Sample	Step 1 Saponification	Step 2 End-chain functionalization	Step 3 In-chain epoxidation	Description
JCO	JCO	X	x	x	Jatropha Crude Oil (JCO)
OA	OA	X	x	x	Oleic acid (OA)
LA	LA	X	x	x	Linoleic acid (LA)
SIL	Silane	X	x	x	Silane* (SIL)
JCO_S_1	JCO	V	x	x	Standard saponification of JCO
JCO_S_2	JCO	V	x	x	Standard saponification of JCO
JCO_F	JCO	X	v	x	End-chain functionalization of JCO
OA_F	OA	X	v	x	End-chain functionalization of OA
LA_F	LA	X	v	x	End-chain functionalization of LA
JCO_SF_1	JCO	V	v	x	End-chain functionalization of JCO_S_1
JCO_SF_2	JCO	V	v	x	End-chain functionalization of JCO_S_2
JCO_E1	JCO	X	x	v	In-chain epoxidation of JCO method 1
JCO_E2	JCO	X	x	v	In-chain epoxidation of JCO method 2
JCO_SFE2	JCO	V	v	v	In-chain epoxidation of JCO_SF_2

Silane* (3-Glycidyloxypropyl)triethoxysilane.

and 50 g of JCO were added into the balloon and stirred at 65 °C for 2 h. After saponification, 200 mL of distilled water were added. The solution was then poured into a separating funnel, and the unsaponifiable fraction was separated by extraction with 100 mL of hexane (the lower layer was collected). The collected aqueous alcohol phase, containing the soaps, was acidified to pH 1 with HCl (37% v/v). The solution was then poured into a separating funnel, and the free fatty acids (FFAs) were recovered by extraction with hexane (the upper layer was collected). The extracted FFA-containing fraction was washed in a separating funnel with distilled water until reaching a neutral pH and then dried in a vacuum rotary evaporator at 35 °C, 340 Pa, and 100 rpm. The procedure was based on the one proposed by Salimon et al.[54] Saponified JCO samples were designated with S in their identification codes (see Table 2 for oil samples and **Table 3** for panel samples).

End-Chain Functionalization with a Silane Precursor

End chain functionalization (step 2) was carried out on different oils (JCO, OA, LA), pristine or after saponification (step 1). 50 g of oil sample and 10 g of SIL were added to the balloon in the same synthesis setup described above. The system was stirred at 60 °C for 6 h and left in agitation overnight at room-temperature. Finally, the sample was collected and used without further purification. End-chain functionalized oil samples were designated with F in their identification codes (see Table 2 for oil samples and Table 3 for panel samples).

In-Chain Epoxidation

In-chain epoxidation reactions (step 3) were carried out on different JCO samples, pristine or after saponification (step 1) + end-chain functionalization (step 2), according to two different methods.

Epoxidation: Method 1

50 g of oil sample and 26 mL of glacial acetic acid were added into the balloon in the same synthesis setup described above and stirred at 525 rpm at room-temperature. 88 mL of hydrogen peroxide maintained at 10 °C was supplied dropwise to the stirred solution and heated at 60 °C for 5 h. The sample was washed with a 3 M sodium chloride solution in a separating funnel until reaching a neutral pH. The residual product was purified in a vacuum rotary evaporator. For more information, refer to Bhakri et al.[55]

Oil samples epoxidized with method 1 were designated with E1 in their identification codes (see Table 2 for oil samples).

Epoxidation: Method 2

200 g of oil sample, 51 g of ion exchange resin Dowex 50WX2 (0.6 meq mL^{-1}), and 26 g of acetic acid (molar ratios of H_2O_2/C=C=1.7:1 and CH_3COOH/C=C=0.8:1) were added to the balloon in the same synthesis setup and agitated at 1400 rpm and 75 °C for 10 min. 32 g of hydrogen peroxide at 30% wt. was added dropwise to the solution, maintaining the reaction temperature at 75 °C, and then stirring it for 5 h. These parameters are indicated by Malarczyk-Matusiak et al.[56] as the optimized synthesis for the conversion and selectivity of the epoxidation process. The ion exchange resin was filtered out, and the sample was purified in a vacuum rotary evaporator at 35 °C, 340 Pa, and 100 rpm. Oil samples epoxidized with method 2 were designated with E2 in their identification codes (see Table 2 for oil samples and Table 3 for panel samples).

2.3. Preparation of Wood Particle Board (PB)

Wood PBs were prepared by compounding different resins with hemp or poplar wood chips, designated with H or P, respectively, in panels' identification codes (see Table 3). The resins were obtained by mixing three components:

Table 3. Panels' Descriptions and Codes.

Sample Identification Code	Wood chips amount [%]	Wood chips	Resin amount [%]	Resin Composition		
				MUF amount [%] [MUF type]	JSK biodispersion [%]	JCO amount [%] [JCO sample]
H_100UF1_01	93	Hemp	7	100 (11G300)	0	0
H_100UF2_01	93	Hemp	7	100 (11H328)	0	0
H_50UF1_50B_01	93	Hemp	7	50 (11G300)	50	0
H_50UF1_40B_10J_01	93	Hemp	7	50 (11G300)	40	10 (JCO)
H_50UF1_40B_10E2_01	93	Hemp	7	50 (11G300)	40	10 (JCO_E2)
H_50UF1_40B_10SFE2_01	93	Hemp	7	50 (11G300)	40	10 (JCO_SFE2)
P_100UF1_01	93	Poplar	7	100 (11G300)	0	0
P_100UF2_01	93	Poplar	7	100 (11H328)	0	0
P_100UF2_02	93	Poplar	7	100 (11H328)	0	0
P_100UF2_03	96.5	Poplar	3.5	100 (11H328)	0	0
P_50UF1_50B_01	93	Poplar	7	50 (11G300)	50	0
P_50UF1_40B_10J_01	93	Poplar	7	50 (11G300)	40	10 (JCO)
P_50UF1_40B_10E2_01	93	Poplar	7	50 (11G300)	40	10 (JCO_E2)
P_50UF1_40B_10SFE2_01	93	Poplar	7	50 (11G300)	40	10 (JCO_SFE2)
P_50UF1_30B_20SFE2_01	93	Poplar	7	50 (11G300)	30	20 (JCO_SFE2)
P_50UF2_40B_10J_01	93	Poplar	7	50 (11H328)	40	10 (JCO)
P_50UF2_40B_10E2_01	93	Poplar	7	50 (11H328)	40	10 (JCO_E2)
P_50UF2_40B_10SFE2_01	93	Poplar	7	50 (11H328)	40	10 (JCO_SFE2)
P_50UF2_40B_10SFE2_02	93	Poplar	7	50 (11H328)	40	10 (JCO_SFE2)
P_50UF2_30B_20E2_01	93	Poplar	7	50 (11H328)	30	20 (JCO_E2)
P_50UF2_30B_20SFE2_01	93	Poplar	7	50 (11H328)	30	20 (JCO_SFE2)
P_50UF2_20B_30E2_01	93	Poplar	7	50 (11H328)	20	30 (JCO_E2)
P_50UF2_20B_30SFE2_01	93	Poplar	7	50 (11H328)	20	30 (JCO_SFE2)
P_20UF2_50B_30E2_01	93	Poplar	7	20 (11H328)	50	30 (JCO_E2)
P_20UF2_50B_30SFE2_01	93	Poplar	7	20 (11H328)	50	30 (JCO_SFE2)
P_0UF_80B_20E2_01	93	Poplar	7	0	80	20 (JCO_E2)
P_0UF_80B_20SFE2_01	93	Poplar	7	0	80	20 (JCO_SFE2)

i. A synthetic UF-based component, either MUF 11G300 or MUF 11H328, combined with an ammonium sulfate-based catalyst (20% solid content) at a 100:1 ratio. These were designated with UF1 or UF2, respectively, in panels' identification codes (see Table 3).
ii. A bioderived JSK-based biodispersion, designated with B in panels' identification codes (see Table 3).
iii. A bioderived pure or modified JCO component, designated with J or S and/or F and/or E, in panels' identification codes (see Table 2 for oil samples and Table 3 for panel samples).

Resin Preparation

5.2 g of pure or chemically modified JCO were added to 94.8 g of water-based biodispersion obtained from crushed JSK (B). After adding the reactants, the compound was stirred with a mechanical stirrer (ARGO LAB AM 20D) at 220 rpm for 1 min and then at 1000 rpm for 5 min. The resulting bioderived mixture was then mixed with UF to obtain the resin, following the UF/B/JCO ratios specified in Table 3 coding system.

Wood PB Production

Virgin poplar chips (P) and virgin hemp chips (H), both suitable for surface finishing, were used for PB fabrication. Traditional PB panels are typically manufactured with a sandwich structure (with core chips bigger than surface chips) to enhance internal strength for furniture applications. However, since the primary goal of this work was to scribe LIG on the panel surface, the sandwich structure was omitted to simplify manufacturing and focus on surface finishing that usually uses short fibers.

The chips were dried for 48 h at 75 °C in an oven before forming, reaching a moisture content of ≈4%.

PB (195 mm × 195 mm area, 15 mm average thickness, target density 500 kg m^{-3}) were manufactured by mixing the wood chips and the resin and then hot pressing the composite at 110 °C for 150 s (Nicem P-LAB 100 T laboratory press).

Twenty-seven PB panels were produced with different compositions and resination percentages, with descriptions and codes listed in Table 3. Predicted moisture content is evaluated and reported in Table S1 (Supporting Information).

2.4. Laser-Induced Graphene

A UV laser engraver (Keyence MD-U1000C, P_{max} = 2.5 W, laser emission wavelength λ = 355 nm, nominal beam size 2 µm) was used to create LIG patterns on all tested materials. The laser scribing was carried out in ambient conditions. The laser was operated in slant left-to-right mode, with laser settings: power P = 60–70%, speed S = 10 mm s^{-1}, pulse frequency = 210 kHz, spot variable = -60, filling 0.010–0.015 mm, 1 repetition.

2.5. Jatropha Crude Oil Characterization

FTIR

FTIR spectra of the materials were recorded with a Shimadzu IR Affinity-1 instrument equipped with a universal ATR (Attenuated Total Reflection) accessory (MIRacle 10). One drop of each oil sample was placed on the crystal surface using a pipette. Mid-IR spectra were obtained by averaging 64 scans over the range 4000–600 cm^{-1} at 4 cm^{-1} resolution.

Titration for Acid Content

Method NGD C10-1976[57] was exploited to obtain the acid content (choosing a normality $N = 0.5$ eq l^{-1}). The molecular weight of JCO has been evaluated based on the data obtained from the specific sample used (Table S2, Supporting Information), and it is in line with the values found in the literature.[58,59] The value of the full triglyceride molecular weight (870.11 g mol^{-1}) was used for the pristine JCO samples; instead, the value of the average single fatty acid molecular weight (277.37 g mol^{-1}) was used for the JCO_S samples. JCO samples from chemical reactions after saponification were assumed to maintain the same molecular weight.

2.6. Wood Particle Board Characterization

Thickness Swelling Test

Thickness swelling tests on panel samples were performed according to EN 317_1993 norm to measure the thickness swelling exposed to water. Briefly, test specimens measuring 50 mm × 50 mm must be pre-conditioned in a controlled environment at (20 ± 2) °C and (65 ± 5)% relative humidity until they reach a constant mass. After conditioning, the initial thickness is measured, and the samples are then fully submerged in water at (20 ± 1) °C for 24 h. The thickness is measured again immediately after removal, and the swelling percentage is calculated based on the difference between the initial and final thickness values.

Internal Bonding Strength Test

Mechanical tests to assess the internal bonding strength (IB) of the panel samples were performed according to the ASTM D1037 standard. Briefly, specimens measuring 50 mm × 50 mm were conditioned at (20 ± 3) °C and (65 ± 5)% relative humidity until reaching constant mass. The test was conducted using a universal testing machine, applying a tensile load perpendicular to the panel surface at a constant rate until failure. The IB strength was calculated as the maximum load at failure divided by the specimen's cross-sectional area.

2.7. Laser-Induced Graphene Characterization

Microscopic Characterization

LIG morphology was investigated with a Hirox HR 5000 (E) digital optical microscope equipped with High-Range Motorized Triple Zoom Lens, and with a Phenom XL SEM (ThermoFisher Scientific) equipped with EDS/EDX and operating at 10 kV. Non-conductive samples were coated with a 10 nm-thick Au-Pd layer using a sputter-coater (Quorum), enabling SEM imaging.

Raman Spectroscopy

The Raman spectroscopy was carried out with a LabRAM HR Evolution Raman microscope at a wavelength of λ_i = 532 nm, with a power percentage of 3.2% (nominal power = 3.2 mW). An integration time of 3 s per 10 accumulations, a slit size of 300 µm, and a ×100_VIS objective were used. The obtained raw data were then post-processed with peak-conservative smoothing, baseline correction, normalized over I_G, and averaged over three samples. The peak ratios I_D/I_G and I_{2D}/I_G were obtained from the post-processed spectra.

The I_D/I_G ratio was used to evaluate the crystalline size, according to Equation (1).[60]

Equation (1) Crystalline size L_a formula.

$$L_a\ (\text{nm}) = \left(2.4 \cdot 10^{-10}\right) \lambda_i^4 \left(\frac{I_D}{I_G}\right)^{-1} \tag{1}$$

Sheet Resistance

Square-shaped patterns (L = 10 mm) were laser-scribed onto panels I and III for electrical characterization. Sheet resistance was measured using a four-point probe system plugged into a Keithley 2604B, with four equally spaced, collinear probes positioned at the center of each square. The probe spacing was s = 2.75 mm. Although LIG thickness was not measured, prior studies report thicknesses in the order of tenths to hundreds of µm, while our probe spacing was in the order of mm, thereby justifying the use of a thin-film approximation. A source current of 1 mA was applied, and the resulting voltage drop between the inner probes was recorded. The sheet resistance R_s was calculated using Equation (2) and corrected by a geometric factor k, accounting for the finite size and square shape of the samples. Based on a probe spacing-to-side length ratio ($s/L \approx 0.3$) and central probe placement, the correction factor was set to $k = 0.5422$.[61] Each reported value represents the average of at least three measurements per panel type.

Equation (2) Sheet Resistance R_s formula.

$$R_s\ \left(\Omega\square^{-1}\right) = \frac{\rho}{t} = \frac{\pi}{ln\,(2)}\ \frac{V}{i}k \tag{2}$$

Applications of Laser-Induced Graphene

A LIG circuit was obtained on a 50 mm × 50 mm panel IV – P_50UF2_40B_10SFE2_01, with the same laser setting reported above. The conductive LIG tracks were 4 mm wide and 40 mm long; the tracks between the LEDs were 4 mm wide and 5 mm long. Connections between the LIG tracks and commercial LEDs have been made with screen-printable stretchable silver paste spread with a brush and cured at 100 °C for 15 min. Electrical contacts for connections to the power supply have been obtained with the same silver paste applied on a Polyimide sheet and cured at 100 °C for 15 min.

Interdigitated humidity sensors (length 40 mm, height 20 mm, thickness and spacing of digits 1 mm) were obtained with the same laser setting on different 50 mm × 50 mm panels (panel I – P_100UF2_03, panel II – P_100UF2_02, and panel III – P_0UF_80B_20SFE2_01). Connections and electrical contacts for the power supply were obtained using the same technique.

The humidity sensors were conditioned and tested in a climatic chamber (ESPEC 242 SH) with an LCR meter (BK Precision 895) by recording the capacitance C over time at AC 1000 kHz through a custom-made Python interface. The imposed relative humidity (*RH*) protocol consisted of an initial conditioning phase, followed by 30 min of data acquisition at RH = 40%, a 10 min ramp to increase RH to 90%, 20 min of data acquisition at RH = 90%, a 10 min ramp to decrease RH back to 40%, and a final 30 min data acquisition at RH = 40%. The temperature was kept constant at T = 25 °C for the whole duration of the tests. The hysteresis error E_H was defined as reported in Equation (3), with C_i and C_f being the sensor capacitance at RH = 40% at the beginning and the end of the protocol, respectively.

Equation (3) Hysteresis error E_H formula.

$$E_H = \frac{\left|C_f - C_i\right|}{C_i} \cdot 100 \tag{3}$$

The sensitivity S of the sensor was defined as shown in Equation (4), where $C_{@40\%}$ and $C_{@90\%}$ represent the sensor capacitance at RH = 40% and RH = 90%, respectively. These values were calculated by averaging the capacitance measurements over the central 10 min of the initial RH = 40% and RH = 90% intervals.

Equation (4) Sensitivity S formula.

$$S = \frac{\left|C_{@40\%} - C_{@90\%}\right|}{90\% - 40\%} \tag{4}$$

3. Results

This section presents the results in three parts. First, the chemical modifications of the oil samples are analyzed, with changes in FTIR spectra and acid content evaluated through titration experiments. Next, the mechanical properties of PB panels incorporating bioderived resins derived from selected oil samples are examined, focusing on thickness swelling and internal bonding. Finally, the characterization of LIG formed on the panel surfaces is detailed, including morphological analysis and Raman spectroscopy. Two proof-of-concept applications are demonstrated to showcase the excellent conductivity of LIG and its potential for integrating embedded electronics.

3.1. Jatropha Crude Oil

FTIR

Standard Saponification: In all FTIR characterizations, the peaks observed in the spectra at 3000–2700 cm^{-1} are excluded from the analysis, as they were consistent across all samples and are attributed to systemic features. Additionally, the peaks at wavenumbers below 800 cm^{-1} are excluded from the analysis due to potential interferences with the ATR crystal, which result in unclear information.

For what concerns saponification (**Figure 2a**), the FTIR spectra of JCO and JCO_S are compared to those of the pure oleic and linoleic acids (the predominant fatty acids of JCO).[38] Since the saponified JCO_S mostly consists of free fatty acid, similarities in the spectral features between the commercial MUFA and PUFA and the JCO_S samples are expected. Indeed, the peak observed at 1744 cm^{-1} in pure JCO, associated with the C═O double bond stretching vibration in esters, disappears, whereas the band at ≈1707 cm^{-1}, associated to C═O in acidic moieties, results well evident in both JCO_S, OA, and LA. This shift is indicative of the cleavage of ester bonds in triglycerides during saponification, resulting in the formation of free fatty acids, and in particular carboxylic acids.[54,62–65] The effectiveness of the reaction is further reinforced by the disappearance of the ester-associated peak at 1159 cm^{-1}, originally present in pure JCO due to the C—O stretching vibration,[54,63,65] and by the emergence of two new peaks in JCO_S at 1285 and 936 cm^{-1}, corresponding to the C—O asymmetric stretch and O—H bending vibration of carboxylic acids, respectively.[54] These spectral changes provide clear evidence that the saponification process is effective.

End-Chain Functionalization by Using a Silane Precursor: For what concerns end-chain functionalization (Figure 2b,c; Figure S1a,b, Supporting Information), the spectra of all end-chain functionalized samples clearly show the existence of the silane compound peaks at 1165 (asymmetric stretching of the C—O—C epoxy rings[66] that is already present in the silane precursor structure),[66] 1099 (stretching of Si—O—C bond),[67] 1074 (asymmetric stretching of Si—O—Si bonds),[68] 953 (stretching vibration of Si—OH),[66,67] and 911 cm^{-1} (asymmetric stretch of C—O—C of the epoxy ring).[69] The silane compound peaks appear independently of the starting sample, and indeed, the difference between a non-saponified (JCO) and a saponified (JCO_S, OA, LA) sample is still evident even after the functionalization with a silane precursor (JCO_F and JCO_SF, OA_F and LA_F, respectively). Since the end-chain functionalization is supposed to happen at the end of the fatty acid chain, formerly bonded to the glycerol, it should not work in a non-saponified JCO. However, the pattern peaks associated with silane-related groups are still present in the spectra of non-saponified samples JCO_F (Figure 2b). This questions whether the silane is bonded to the chain or simply in solution.

A possible answer to the question can be given in Figure S1c (Supporting Information), comparing a saponified and functionalized JCO_SF with the same sample after further epoxidation

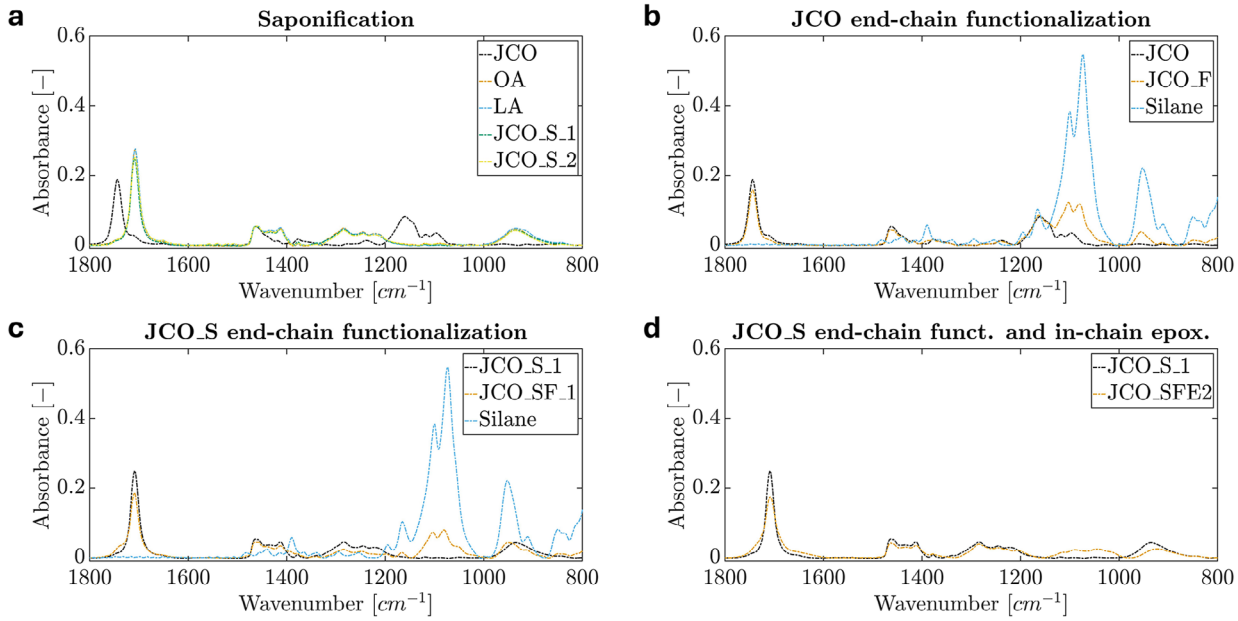

Figure 2. FTIR spectra of oil samples: a) pure JCO, OA, and LA and saponified JCO samples; b) pure JCO, end-chain functionalized pure JCO, and silane samples; c) saponified JCO, end-chain functionalized saponified JCO, and silane samples; d) saponified JCO before and after end-chain functionalization and in-chain epoxidation.

JCO_SFE2. The pattern peaks of silane functionalization disappear after epoxidation, probably because this process involves washing and evaporation steps, which may have carried away the unbonded silanes.

In-Chain Epoxidation: Two methods were adopted for in-chain epoxidation (Figure S1d, Supporting Information).

The first method[55] does not show any results, as samples JCO and JCO_E1 do not show any difference in their FTIR spectra.

The second method[56] also does not show any significant difference before and after the epoxidation of pure JCO (JCO and JCO_E2). The minor difference observed (lowering of the signal intensity in the region ≈1100 cm^{-1}) is insubstantial and allows us to conclude that epoxidation did not work in non-saponified JCO. However, the second epoxidation method was also applied to saponified and end-chain functionalized JCO_SF (Figure S1c, Supporting Information). Differences between JCO_SF and JCO_SFE2 are observed in the 1300–800 cm^{-1} range, particularly in the significant reduction of bands at 1167, 1103, 1080, and 949 cm^{-1}. While this decrease may be attributed to the removal of the unbound silanes that remained after the end-chain functionalization, samples JCO_S_1 and JCO_SFE2 still exhibit distinct spectral features in the 1300–800 cm^{-1} range (Figure 2d). This suggests that, in this case, the epoxidation reaction may have worked, but this process needs to be investigated further in future works since these peaks are not clearly recognizable and the starting sample can probably influence the efficiency of the process. Thus, only the samples obtained with this second epoxidation method (indicated with "E2") are used for wood panel manufacturing.

In summary, spectroscopic analyses showed that the saponification reaction worked and that further investigations are needed to evaluate and optimize end-chain functionalization by using silane as a precursor and in-chain epoxidation.

Titration for Acid Content

Table 4 shows the free fatty acid (FFA) content in each sample. It can be observed that pure JCO has an FFA content of 16%, meaning that there are some free fatty acids even in the starting sample (although they are not detectable in FTIR spectra, Figure 2). However, both JCO samples after saponification report a large increase in acid content (which reached FFA > 90%), confirming the successful saponification.

3.2. Production of Wood Particle Board Panels

The physical and mechanical properties of the panels are evaluated, with results summarized in **Table 5**. Additional data on thickness swelling (Table S3, Supporting Information) and internal bonding (IB) strength (Table S4, Supporting Information) are included in the Supporting Information.

Comparison of Poplar and Hemp Panels

Poplar and hemp panels exhibit similar overall trends, but the mechanical performance of hemp panels is notably inferior. Indeed, hemp samples show significantly lower IB strength than their poplar counterpart (e.g., 0.017 MPa vs 0.362 MPa for the 100UF2 series, Table 5). Moreover, thickness swelling is significantly higher, numerous cracks develop during the tests, and samples release dark brown substances into the water. As a result, further testing is only carried out on poplar panels.

Table 4. Free fatty acid (FFA) content of pure and saponified JCO samples.

Sample Identification Code	Molecular Weight [g mol^{-1}]	Mass [g]	Volume [l]	FFA content [%]
JCO_1	870.11	2.52	0.0009	16%
JCO_S_1	277.37	2.49	0.0163	91%
JCO_S_2	277.37	2.54	0.0177	97%

Impact of Resin Composition

Substituting UF1 with UF2 significantly improves swelling resistance and yields the best mechanical performance across all formulations in fully synthetic samples (P_100UF1 vs P_100UF2), in line with what is expected from literature for MUF with higher melamine content.[37] Partially replacing half of the synthetic UF with JSK biodispersion and different JCO samples (P_50UFx_yB_01, using J, SFE2, and E2) results in a significant reduction of IB strength compared to the 100% synthetic reference. For the UF1-based series, the IB strength decreases from 0.152 to 0.088 MPa, while for the UF2-based series from 0.362 to 0.100 MPa. Thickness swelling increases notably in the UF2-based series when the JSK biodispersion is added, whereas the UF1-based series shows only a minor change. Nevertheless, the UF1-based series exhibits generally poor dimensional stability, even at 100% synthetic content (26.8% vs 28.2% for full synthetic and half synthetic samples, respectively), in contrast to the better overall performance of the UF2-based series (18.0% vs 27.4% for full synthetic and half synthetic samples, respectively).

It is worth noting that the panels made with various amounts of JSK biodispersion and different JCO samples (J, E2, and SFE2) show similar IB strength, meaning that the bioderived components interact with the UF in a mechanically detrimental way regardless of their relative amount (20–50% of JSK and 0–30% of J, E2, and SFE2). The absence of difference among the samples with bioderived components is probably due to their relatively low absolute amount, which may mask their effect on matrix bonding. When looking specifically at panels made with JCO_SFE2, the mechanical performances decrease only for the UF1-based series (IB = 0.040 MPa, thickness swelling 34.4%), whereas for the UF2-based series, they are similar to the other partially bioderived combinations.

Performance of Fully Bioderived Panels

Panels with 100% bioderived resin (P_0UF_80B_20E2_01, P_0UF_80B_20SFE2_01) lack mechanical stability. While they maintain a homogeneous external surface, the core is poorly bonded and crumbles under stress.

Total Resin Content

Reducing the total resin content (i.e., P_100UF2_03 with 3.5% resin) also compromises performance, indicating that lower resin percentages are unsuitable. However, when considering samples with the same absolute amount of UF inside the panel (e.g., P_100UF2_03 and P_50UF2_40B_10J_01), adding the bioderived compound to the resin may result in increased properties.

General Observations

Increasing the proportion of bioderived compounds consistently results in higher swelling and lower IB strength. Fully bioderived panels are mechanically unstable; however, certain partially bioderived formulations achieve sufficient bonding ($0.08 \leq IB \leq 0.14$) for robust panels suitable for the here-proposed application. Variations in oil type (JCO, E2, SFE2) within the same matrix composition yield similar mechanical properties, at least

Table 5. Moisture content, thickness swelling, and internal bonding strength of the panels. For the Sample Identification Code, "x" is used as a parameter for the B quantity, while "z" is the parameter for the quantity of the different formulations of JCO (J, E2, and SFE2). Where available, average values and standard deviations are reported, based on measurements performed at least in triplicate.

Sample Identification Code	Moisture content [%wt./wt.]	Swelling [%]	IB [MPa]
H_100UF1_01	7.4	50.9	NA
H_100UF2_01	7.2	28.9	0.017
H_50UF1_xB_z	12.9 ± 0.8	40.7 ± 3.8	0.022 ± 0.004
P_100UF1_01	7.4	26.8	0.152
P_100UF2	7.2 ± 0.0	18.0 ± 0.1	0.362 ± 0.072
P_50UF1_xB_z	13.0 ± 0.9	28.2 ± 1.5	0.088 ± 0.012
P_50UF1_xB_zSFE2	11.7 ± 1.2	34.4 ± 5.4	0.040 ± 0.005
P_50UF2_xB_z	11.2 ± 1.6	27.6 ± 4.0	0.099 ± 0.025
P_50UF2_xB_zSFE2	11.2 ± 1.6	31.3 ± 5.5	0.091 ± 0.016
P_20UF2_50B_30z	13.1 ± 0.0	37.7 ± 2.0	0.013 ± 0.005

for UF2-based series, suggesting that the absolute oil content is often insufficient to significantly influence bonding. However, increasing the proportion of bioderived matrix may have the potential for achieving properties comparable to 100% UF-based panels.

3.3. Laser-Induced Graphene

This section presents the results of various representative characterization of LIG obtained from three selected panel formulations: panel I – P_100UF2_03 (100% UF2 at 3.5% resination), panel II – P_100UF2_02 (100% UF2 at 7% resination), and panel III – P_0UF_80B_20SFE2_01 (100% bioderived compound at 7% resination). These panels' formulations were selected as they were representative of the use of only synthetic resin (panels I, II, varying for resination amount) and only bioderived one (panel III). Additionally, the application subsection includes data from panel IV – P_50UF2_40B_10E2_01 (50% UF2, 50% bioderived compound at 7% resination).

Microscopic Characterization

The morphology of LIG is usually characterized by distinct features resulting from the laser scribing process. The Gaussian intensity profile of the laser beam spot creates a gradient in fluence transversal to the scribing direction, and hence differences are observed within the so-called Heat Affected Zone.[70] A higher degree of crystallinity of the carbon material is observed at the center of the scribed area, which decreases toward the edges.[71] Additionally, and for similar reasons, LIG exhibits a layered structure across its thickness, with a highly graphitized top layer on the surface, transitioning into an amorphous carbon layer going downwards.[70]

Here, the microscopic structure of the panel-derived LIG (**Figure** 3g–o) consists of pores and fiber entanglements, resembling PI-derived LIG but with greater disorder.[1] This increased disorder may arise from three factors: first, the inherent wood anatomy, influenced by factors such as wood type (softwood or hardwood), density, and xylem structure (which determines porosity);[18] second, the surface morphology of the panels before scribing (Figure 3a–f), characterized by high and irregular roughness, due to the dimensions of the chips;[18] third, the structural integrity of the panel, which should not present loosely attached surface chips. Indeed, the latter can lead to a loss of LIG material, an exposure of the underlying wood after scribing, and a consequential decrease in performance. In this case, it especially happened for the bioderived panels (Figure 3i), in agreement with the mechanical properties, which show a lower internal bonding with increasing bioderived compound percentages. The electrical resistance of laser-scribed LIG tracks per unit length is similar for all the panels and is $R \approx 700\ \Omega\ \mathrm{cm}^{-1}$. It is important to notice that these values are taken on LIG scribed in the smoother areas of the panels, when possible, to limit the influence of the morphological changes of the substrate and reduce the physical interruptions of the conductive path, due to excessive roughness or loosely bound chips.

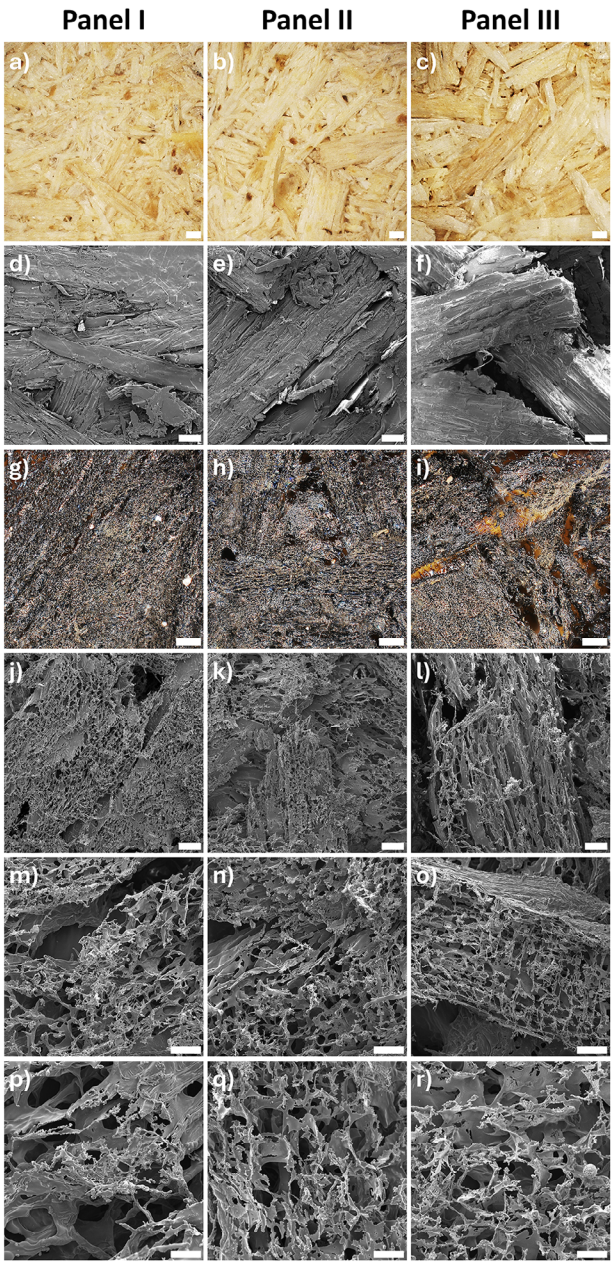

Figure 3. Optical images of synthetic and bioderived pristine panels: a) panel I; b) panel II; c) panel III (the scalebar is 500 μm). SEM images of synthetic and bioderived pristine panels: d) panel I; e) panel II; f) panel III (the scalebars are 100 μm). Optical images of LIG obtained from synthetic and bioderived panels: g) panel I; h) panel II; i) panel III (the scalebar is 200 μm). SEM images of LIG obtained from synthetic and bioderived panels: j) panel I; k) panel II; l) panel III (the scalebar is 100 μm). SEM images of LIG obtained from synthetic and bioderived panels at high magnification: m) panel I; n) panel II; o) panel III (the scalebar is 40 μm); and p) panel I; q) panel II; r) panel III (the scalebar is 20 μm).

Sheet Resistance and Raman Spectroscopy

LIG obtained from panels I (P_100UF2_03, i.e., 7% resination, 100% synthetic-based) and III (P_0UF_80B_20SFE2_01, i.e., 7% resination, 100% bioderived) are used for sheet resistance and

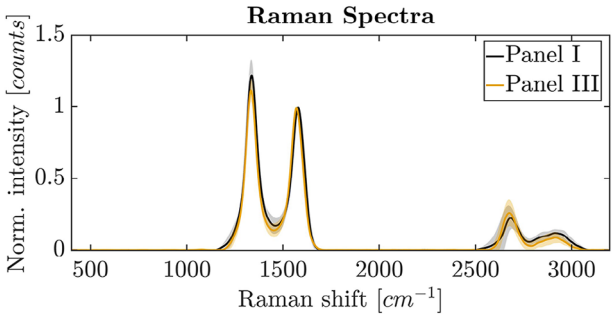

Figure 4. Raman Spectra of LIG scribed on Panel I and Panel III. Solid lines represent the average normalized intensity across three samples, while shaded regions indicate the standard deviation.

Raman spectroscopy to assess the impact of resin composition on LIG. Indeed, the two panels with the most different resins have been chosen for this test. Although the measured sheet resistance values R_s are higher than those reported in the comparison table, it is important to highlight that most of the referenced studies do not specify the formulas or experimental setups used to determine sheet resistance, making direct comparison difficult. Panels I and III exhibited values on the same order of magnitude, with average sheet resistance of 322 Ω $\square^{-1}$ and 425 Ω $\square^{-1}$, respectively. Nevertheless, multimeter measurements yielded consistent and satisfactory results, on the order of a few hundred Ω cm^{-1}.

The Raman spectra obtained (**Figure 4**) show the three D, G, and 2D distinct bands of graphenic/graphitic materials,[1][72] for both panels. Small shifts of peaks are observed with peaks at D = 1337 and D = 1334 cm^{-1}, G = 1579 and G = 1570 cm^{-1}, and 2D = 2683 and 2D = 2675 cm^{-1}, for panel I and panel III, respectively. The intensity ratios for panel I are $I_D/I_G = 1.23$ and $I_{2D}/I_G = 0.22$, while for panel III are $I_D/I_G = 1.12$ and $I_{2D}/I_G = 0.26$. The I_D/I_G ratio is known to be proportional to the defects in the hexagonal structure of graphene; thus, a lower value is associated with a less defective structure.[73] The I_D/I_G ratio can be used to evaluate the crystalline size, according to Equation (1) (Experimental Section), and it is found to be $L_a = 16$ and 17 nm, for panels I and III, respectively. Instead, I_{2D}/I_G is inversely related to the number of stacked graphene layers, with monolayer graphene having $I_{2D}/I_G \geq 2$.[74] Overall, panel III exhibits slightly improved Raman spectra compared to panel I, with a lower I_D/I_G and a higher I_{2D}/I_G ratio, indicating a less defective planar structure and reduced layer stacking. However, the differences remain minimal, likely due to the extremely low resin content in both panels (3.5% and 7% for Panel I and III, respectively) relative to the wooden chips, despite their significantly different matrix compositions. It is important to notice that recording Raman spectra from these samples can be challenging. Indeed, they were taken from the most morphologically homogeneous areas of the panels' surface: retrieving Raman spectra in regions with higher and irregular roughness is unfeasible due to the field of view and focal distance limitations of the instrument. Even in the selected areas, challenges can arise due to their limited smoothness, which adds to the constraints imposed by the instrument's field of view and focal distance. It can therefore be hypothesized that using smaller chips would lead to a more uniform and smoother panels' surface and therefore improved Raman peak intensity ratios.

Table 6. Comparison of this work with the literature on wood-derived LIG (pre-treated wood included). Data from this work are reported as average and standard deviation values from triplicate measurements.

Refs.	Sample	I_D/I_G	I_{2D}/I_G	R_s [Ω $\square^{-1}$]
[18]	Ebony wood	≈ 1.2*)	≈ 0.1*)	45
[19]	Wood	0.68	0.32	n.a.
[20]	Oak wood	0.48	≈ 0.6*)	≈ 10
[21]	Sliced spruce veneers	≈ 0.2*)	≈ 0.6*)	≈ 24*)
[22]	Cedar wood	0.3	0.76	< 7
[23]	Pine wood	1.11	0.78	35
[24]	Plywood	≈ 0.7*)	≈ 0.7*)	≈ 8
[24]	Plywood	≈ 0.8*)	≈ 0.4*)	< 5
[25]	Wood	≈ 1.3*)	≈ 0.5*)	10
[25]	Wood	0.67	≈ 0.9*)	10
[26]	Spruce wood	0.92	≈ 0.6*)	18.6
[27]	Bamboo	0.7	≈ 0.5*)	n.a.
[1]	PI	1.2	0.7	15
this work	Panel I	1.23 ± 0.11	0.23 ± 0.08	322 ± 0
this work	Panel III	1.12 ± 0.08	0.26 ± 0.09	425 ± 0

*) Extracted from figures in the reference, because no values were given. n.a., not available.

Compared to the existing literature, the intensity ratios for panel I and panel III are slightly different from those of reference PI-derived LIG (I_D/I_G = 1.2 and I_{2D}/I_G = 0.7).[1] This variation is expected in wood-derived LIG, due to the inherent complexity, structural and chemical variability of biomass compared to PI, which is an industrially developed, highly uniform film/sheet. The peak intensity ratios observed in this study are consistent with those reported for other wood-derived LIG[16,18] (the most relevant results are reported in **Table 6**). While some documented I_D/I_G ratios suggest a less defective structure,[20–22] the LIG scribing proposed in those studies requires an inert atmosphere, chemical pretreatments of precursor substrates, or the addition of flame retardants. Notably, in this work, the wood panels are used as substrates without any pretreatment, controlled atmosphere, or specific laser settings. This approach not only simplifies the production process but also aligns with sustainability principles, reducing the environmental impact and the overall cost of the process.

Applications of Laser-Induced Graphene

Figure 5 demonstrates the potential application of LIG tracks scribed and embedded on panels as electronic tracks for circuit boards, showcasing its feasibility in real-world electronic systems. A representative panel formulation with 50% UF2 and 50% bioderived compound (panel IV) is chosen as substrate for this demonstrator. The LIG circuit successfully connected four LEDs in series, and the series to a voltage/current supply, confirming LIG conductivity and integration capabilities. This demonstrator is developed to highlight the versatility of LIG tracks in forming functional electronic components on sustainable and customizable substrates, e.g., bioderived panels for furniture. The use of

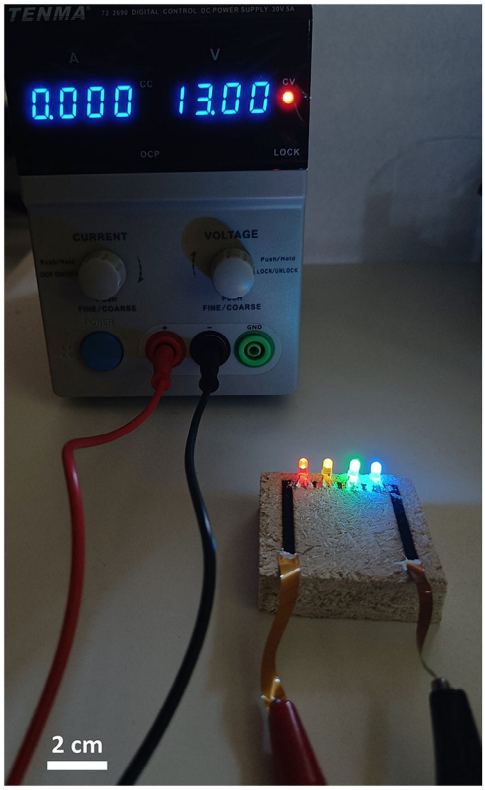

Figure 5. Demonstration of an electric circuit fabricated on panel IV using LIG tracks to power four colored LEDs in series.

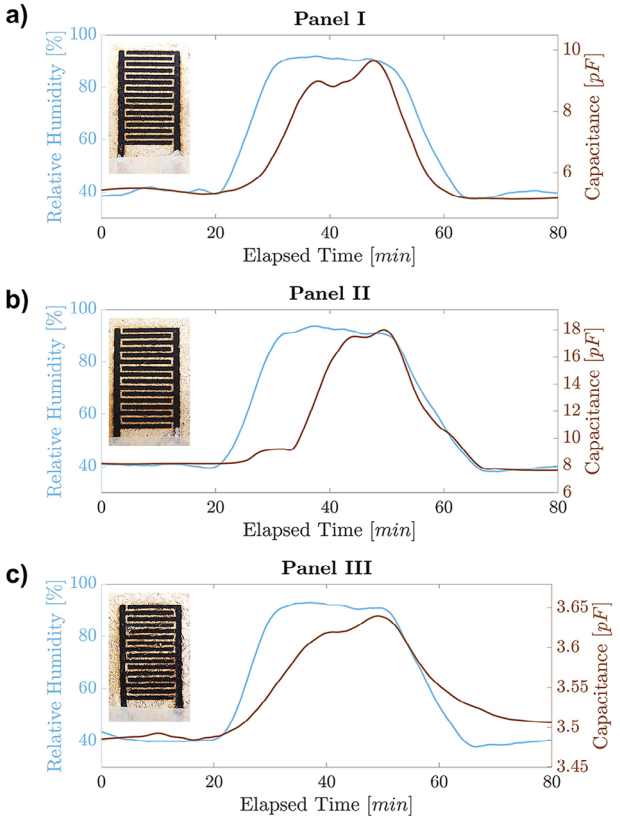

Figure 6. Performances of interdigitated humidity LIG sensors in a controlled environment at T = 25 °C: a) panel I (P_100UF2_03); b) panel II (P_100UF2_02); c) panel III (P_0UF_80B_20SFE2_01). The top-left insets show pictures of the sensors.

LEDs illustrates a practical example of low-power devices that could benefit from such technology.

A second proof-of-concept demonstrator involves the development of a capacitive interdigitated humidity sensor, showcasing the versatility of LIG from bioderived precursors. A first obvious application of this concept could be in embedding environmental humidity monitors in home furniture. Moreover, considering that wood is an inherently hygroscopic material, the ability to monitor the environment and/or panel moisture is critical for preventing issues such as mold growth, rotting, and eventual structure failures. The traditional method for measuring wood moisture relies on a two-point probe system, which assesses the conductivity or capacitance between two metallic probes placed on or inserted into the wood's surface layer.[26] Instead, integrating LIG sensors directly into the panel is particularly advantageous due to their non-invasive nature, possible miniaturization, and monolithic integration. Owing to their direct fabrication on the composite surface, the sensors are inherently integrated into the panel structure, and maintain mechanical stability as long as the underlying substrate remains intact. This approach addresses the increasing demand for embedded, unobtrusive sensing technologies in smart construction materials. It demonstrates an innovative bioderived solution for real-time moisture monitoring, enabling safer and more efficient use of wood in modern construction.[26] An in-depth characterization of the sensor is outside the scope of this paper, but preliminary results are presented here. Three panels are chosen for this test: panel I serves as a reference for composite materials with a low resination percentage (3.5%) and features a 100% UF2-based resin. Panels II and III have a higher resination percentage (7%) and are chosen here to compare the two most different resin formulations (100% UF2 for panel II and 100% bioderived compound for panel III).

Figure 6 illustrates the behavior of humidity sensors scribed on the three panels during a cyclic relative humidity (RH) test, which involves increasing environmental RH from 40% to 90%, a 20 min pause, and a subsequent decrease. Sensors are tested to measure surface moisture absorbed from the external air, but moisture inside the panels can also be easily measured by just encapsulating the sensors to seal the sensing area from the external environment.[26]

All sensors exhibit a cyclic capacitance behavior, which is proportional to the relative humidity, indicating their responsiveness to *RH* changes. The capacitance behavior of humidity sensors scribed on the three panels reveals distinct trends in sensitivity and hysteresis error. The sensor on panel I (Figure 6a) demonstrates good performance, with a sensitivity of $S \approx 0.0959$ pF %RH^{-1}. It also shows rapid response and minimal hysteresis error of $E_H \approx 5\%$. Similarly, the sensor on panel II (Figure 6b) exhibits a comparable hysteresis error of $E_H \approx 5\%$, while slowing the response. However, it outperforms panel I in terms of sensitivity, achieving $S \approx 0.2031$ pF %RH^{-1}. In contrast, the sensor on panel III (Figure 6c) shows a significantly reduced sensitivity

of $S \approx 0.0045$ pF %RH^{-1}. Despite this, it retains a good response speed and shows a lower hysteresis ($E_H \approx 1\%$). A comparison with state-of-the-art petrol-derived and bioderived LIG-based *RH* sensors is provided in Table S5 (Supporting Information).

These results demonstrate that the two 100% UF2-based wood panels (panels I and II) exhibit comparable performance and perform better than the 100% bioderived panel (panel III). However, given the limited amount of resin, this performance difference can be attributed to the rougher surface morphology and lower bonding stability of the bioderived panel. These factors are indirectly influenced by the resin used but are not directly related to the possibility of scribing LIG on top of the panels: indeed, the mechanical stability of the substrate, which also depends on the strength of the resin, significantly affects the capacitive behavior of the planar interdigitated sensor. Nonetheless, the capacitance trend over *RH* observed in panel III indicates that, with further optimization of the panel composition and structure, satisfactory performance can be achieved even for 100% bioderived panels. Moreover, to showcase the potential for future miniaturization, conductive tracks were successfully scribed using a single laser pass on both the wood substrate (panel II) and, as a reference, on polyimide (Figure S2, Supporting Information). The observed difference in the impacted area between the two substrates stems from the laser settings: a defocused beam was employed for the wood panel, leading to a larger spot size. It is worth noting that implementing miniaturized tracks on wood is not always straightforward, depending on the size of the embedded wood chips. When relatively large wood chips are used, the mechanical stability of miniaturized LIG tracks (size comparable with wood chips one) can be compromised by the substrate roughness and delamination risk.

4. Conclusion

This study demonstrates the feasibility of using bioderived components extracted from *Jatropha curcas* L. seeds to reduce the synthetic content of wooden panel resins and subsequently use these substrates for laser-scribed LIG electronics. While panels made entirely from bioderived resin were not mechanically stable with the tested formulation, partially bioderived panels with sufficient matrix-reinforcement bonding were successfully produced, resulting in robust composites ($0.08 \leq IB \leq 0.14$) suitable for the here proposed application. Variations in oil functionalization did not lead to significant differences in mechanical properties, likely due to the relatively low absolute amount of oil, which may mask its effect on matrix bonding. Increasing the bioderived content in the resin could potentially yield panels with mechanical properties comparable to the 100% UF benchmark. It should also be considered that in the present work, fine particles were used, as the primary objective of this work was to scribe LIG on the panel surface. Accordingly, lower mechanical properties are expected in this situation. Conductive LIG was successfully scribed onto 100% bioderived, partially bioderived, and synthetic panels, with demonstrative applications such as circuit tracks and interdigitated humidity sensors.

These results pave the way for developing sustainable alternatives in the field of smart furniture. Future research should focus on:

1) Resin Optimization: improve oil functionalization after saponification to enhance binding properties and increase resin content to the feasibility of a fully bioderived matrix from *Jatropha curcas L.* seeds and alternatives like soy proteins.
2) Panel and LIG improvements: use larger core chips and finer surface chips to improve mechanical properties and LIG scribing quality. Further testing is needed to confirm the resin's role in enabling LIG scribing.

A Life Cycle Assessment should quantify the environmental impact of bioderived panels for LIG electronics, ensuring that the proposed solutions effectively support sustainability goals. In this context, several key aspects for improving the environmental performance can be identified: prioritizing non-virgin wood fibers as raw materials (e.g., recycled fibers, industrial by-products, agricultural residues),[75] minimizing the use of chemicals in the formulation of bioderived resins, and optimizing the energy consumption during panel fabrication. While the energy required for laser scribing is expected to remain relatively constant due to the physical nature of the process, upstream improvements in material sourcing and processing can reduce the overall impact. In conclusion, this work bridges life cycle thinking and innovation by exploring bioderived resins for wooden panel manufacturing and demonstrating the potential for sustainable electronics on these substrates. By adopting alternatives to conventional synthetic matrices, this study takes a meaningful step toward a more eco-friendly future in manufacturing and electronics, as well as smart furniture.

Supporting Information

Supporting Information is available from the Wiley Online Library or from the author.

Acknowledgements

The authors thank Filippo Privitera from Agroils Technologies for JCO production, Dr. Francesca Pignatelli from the Italian Institute of Technology for the use of FTIR, Dr. Virgilio Mattioli for lending the instruments to characterize the moisture sensors, and Dr. Marina Galliani for her help with the characterization. F.G. acknowledges the support of the BRIEF "Biorobotics Research and Innovation Engineering Facilities" project (Project identification code IR0000036) funded under the National Recovery and Resilience Plan (NRRP), Mission 4 Component 2 Investment 3.1 of the Italian Ministry of University and Research funded by the European Union – NextGenerationEU. F.G. acknowledges funding received by the LIGASH Project, funded by the Italian Ministry of Education and Research MUR in the framework of the Fund for the promotion and development of policies of the National Research Program PNR, coherently with EU Regulation n. 241/2021 and with PNRR 2021–2026. A.C.B. acknowledges funding of PhD grant from Programma Operativo Nazionale – PON "Green" Research and Innovation (CCI 2014IT16M2OP005) from the Ministry of Education, University and Research, Italy and FSE React-EU.

Open access publishing facilitated by Scuola Superiore Sant'Anna, as part of the Wiley - CRUI-CARE agreement.

Conflict of Interest

The authors declare no conflict of interest.

Data Availability Statement

The data that support the findings of this study are available from the corresponding author upon reasonable request.

Keywords

bioderived adhesive, Jatropha, laser-induced graphene, PUFA, wood composites

Received: May 6, 2025
Revised: June 19, 2025
Published online:

[1] J. Lin, Z. Peng, Y. Liu, F. Ruiz-Zepeda, R. Ye, E. L. G. Samuel, M. J. Yacaman, B. I. Yakobson, J. M. Tour, *Nat. Commun.* **2014**, *5*, 5714.
[2] T. Beduk, A. Ait Lahcen, N. Tashkandi, K. N. Salama, *Sens. Actuators, B* **2020**, *314*, 128026.
[3] C. Zhang, J. Ping, Y. Ying, *Sci. Total Environ.* **2020**, *714*, 136687.
[4] T.-S. D. Le, H.-P. Phan, S. Kwon, S. Park, Y. Jung, J. Min, B. J. Chun, H. Yoon, S. H. Ko, S.-W. Kim, Y.-J. Kim, *Adv. Funct. Mater.* **2022**, *32*, 2205158.
[5] G. De Luca, A. C. Bressi, R. Pathan, N. Pagliarani, M. Maselli, F. Greco, M. Cianchetti, *Adv. Intell. Syst.* **2025**, 2401071.
[6] W. Ma, J. Zhu, Z. Wang, W. Song, G. Cao, *Mater. Today Energy* **2020**, *18*, 100569.
[7] A. Kaidarova, J. Kosel, *IEEE Sens. J.* **2020**, *21*, 12426.
[8] G. De Luca, A. C. Bressi, M. Maselli, F. Greco, M. Cianchetti, in *2024 46th Annual Int. Conf. of the IEEE Engineering in Medicine and Biology Society (EMBC)*, IEEE, Orlando, FL, USA **2024**, p. 1.
[9] F. M. Vivaldi, A. Dallinger, A. Bonini, N. Poma, L. Sembranti, D. Biagini, P. Salvo, F. Greco, F. D. Francesco, *ACS Appl. Mater. Interfaces* **2021**, *13*, 30245.
[10] Q. Deng, T. Wu, K. Yin, X. Li, L. Wang, Q. Huang, Y. Huang, C. J. Arnusch, J.-A. Duan, *Appl. Phys. Lett.*, *125*, 121602.
[11] L. Wang, K. Yin, Q. Deng, Q. Huang, J. He, J.-A. Duan, *Adv. Sci.* **2022**, *9*, 2204891.
[12] A. Dallinger, F. Steinwender, M. Gritzner, F. Greco, *ACS Appl. Nano Mater.* **2023**, *6*, 16201.
[13] L. Wang, K. Yin, X. Li, Y. Huang, J. Xiao, J. Pei, X. Song, J.-A. Duan, C. J. Arnusch, *Adv. Funct. Mater.* **2025**, 2506215.
[14] K. Yin, D. Chu, X. Dong, C. Wang, J.-A. Duan, J. He, *Nanoscale* **2017**, *9*, 14229.
[15] P. I. C. Claro, T. Pinheiro, S. L. Silvestre, A. C. Marques, J. Coelho, J. M. Marconcini, E. Fortunato, L. H. C. Mattoso, R. Martins, *Appl. Phys. Rev.* **2022**, *9*, 041305.
[16] A. C. Bressi, A. Dallinger, Y. Steksova, F. Greco, *ACS Appl. Mater. Interfaces* **2023**, *15*, 35788.
[17] S. T. Sankaran, A. Dallinger, A. C. Bressi, A. Marino, G. Ciofani, A. Szkudlarek, V. Bilovol, K. Sokolowski, B. Kunert, H. K. Hampel, H. G. Bernal, F. Greco, *Small* **2024**, *20*, 2405252.
[18] S. K. Lengger, L. Neumaier, L. Haiden, M. Feuchter, T. Griesser, J. Kosel, *Sustainable Mater. Technol.* **2024**, *40*, 00936.
[19] S. Dubey, A. S. Thakur, R. Vaish, *FlatChem* **2025**, *52*, 100874.
[20] R. Ye, Y. Chyan, J. Zhang, Y. Li, X. Han, C. Kittrell, J. M. Tour, *Adv. Mater.* **2017**, *29*, 1702211.
[21] C. H. Dreimol, H. Guo, M. Ritter, T. Keplinger, Y. Ding, R. Günther, E. Poloni, I. Burgert, G. Panzarasa, *Nat. Commun.* **2022**, *13*, 3680.
[22] X. Han, R. Ye, Y. Chyan, T. Wang, C. Zhang, L. Shi, T. Zhang, Y. Zhao, J. M. Tour, *ACS Appl. Nano Mater.* **2018**, *1*, 5053.
[23] R. Trusovas, K. Ratautas, G. Račiukaitis, G. Niaura, *Appl. Surf. Sci.* **2019**, *471*, 154.
[24] Y. Chyan, R. Ye, Y. Li, S. P. Singh, C. J. Arnusch, J. M. Tour, *ACS Nano* **2018**, *12*, 2176.
[25] T.-S. D. Le, S. Park, J. An, P. S. Lee, Y.-J. Kim, *Adv. Funct. Mater.* **2019**, *29*, 1902771.
[26] M. Y. Mulla, P. Isacsson, I. Dobryden, V. Beni, E. Östmark, K. Håkansson, J. Edberg, *Glob. Chall.* **2023**, *7*, 2200235.
[27] R. Miyakoshi, S. Hayashi, M. Terakawa, *RSC Adv.* **2022**, *12*, 29647.
[28] S. L. Silvestre, T. Pinheiro, A. C. Marques, J. Deuermeier, J. Coelho, R. Martins, L. Pereira, E. Fortunato, *Flex. Print. Electron.* **2022**, *7*, 035021.
[29] J. Coelho, R. F. Correia, S. Silvestre, T. Pinheiro, A. C. Marques, M. R. P. Correia, J. V. Pinto, E. Fortunato, R. Martins, *Microchim. Acta* **2022**, *190*, 40.
[30] A. Gumowska, G. Kowaluk, *Forests* **2023**, *14*, 84.
[31] S. Boran, M. Usta, E. Gümüşkaya, *Int. J. Adhes. Adhes.* **2011**, *31*, 674.
[32] T. Jiang, D. J. Gardner, M. G. D. Baumann, *For. Prod. J.* **2002**, *52*, 66.
[33] Z. He, Y. Zhang, W. Wei, *Build. Environ.* **2012**, *47*, 197.
[34] D. Cavallo, A. M. Fresegna, A. Ciervo, C. L. Ursini, R. Maiello, V. D. Frate, R. Ferrante, R. Mabilia, B. Pizzo, B. Grossi, P. Ciccioli, P. Ciccioli, S. Iavicoli, *Toxicology* **2022**, *466*, 153085.
[35] M. H. Hussin, N. H. Abd Latif, T. S. Hamidon, N. N. Idris, R. Hashim, J. N. Appaturi, N. Brosse, I. Ziegler-Devin, L. Chrusiel, W. Fatriasari, F. A. Syamani, A. H. Iswanto, L. S. Hua, S. S. A. O. Al Edrus, W. C. Lum, P. Antov, V. Savov, M. A. Rahandi Lubis, L. Kristak, R. Reh, J. Sedliačik, *J. Mater. Res. Technol.* **2022**, *21*, 3909.
[36] B. Grossi, B. Pizzo, F. Siano, A. Varriale, R. Mabilia, *Results Eng.* **2025**, *25*, 104033.
[37] M. Dunky, *Handbook of Adhesive Technology*, *70*, 3rd ed., CRC Press, Boca Raton, FL **2003**.
[38] R. Ejilah, A. Asere, A. Adisa, A. Ejila, *Aust. J. Agric. Eng.* **2010**, *1*, 80.
[39] M. M. Aung, Z. Yaakob, S. Kamarudin, L. C. Abdullah, *Ind. Crops Prod.* **2014**, *60*, 177.
[40] P. Solt, et al., *Int. J. Adhes. Adhes.* **2019**, *94*, 99.
[41] A. P. Singh Chouhan, N. Singh, A. K. Sarma, *Fuel* **2013**, *109*, 217.
[42] B. Y. Lim, R. Shamsudin, B. T. H. T. Baharudin, R. Yunus, *Renewable Sustainable Energy Rev.* **2015**, *52*, 991.
[43] S. Rezania, B. Oryani, J. Park, B. Hashemi, K. K. Yadav, E. E. Kwon, J. Hur, J. Cho, *Energy Convers. Manage.* **2019**, *201*, 112155.
[44] M. H. Duku, S. Gu, E. B. Hagan, *Renewable Sustainable Energy Rev.* **2011**, *15*, 404.
[45] L. C. Cordova-Albores, M. Y. Rios, L. L. Barrera-Necha, S. Bautista-Baños, *Ind. Crops Prod.* **2014**, *62*, 166.
[46] R. A. Babahmad, et al., *Ind. Crops Prod.* **2018**, *121*, 405.
[47] A. Ruggiero, R. D'Amato, M. Merola, P. Valášek, M. Müller, *Proc. Eng.* **2016**, *149*, 431.
[48] N. A. Zainal, N. W. M. Zulkifli, M. Gulzar, H. H. Masjuki, *Renewable Sustainable Energy Rev.* **2018**, *82*, 80.
[49] V. J. Sundar, C. Muralidharan, A. B. Mandal, *Ind. Crops Prod.* **2013**, *47*, 227.
[50] J. M. Jabar, *Curr. Res. Green Sustain. Chem.* **2022**, *5*, 100331.
[51] N. Zain, F. Ghazali, E. Roslin, *Int. J. Mech. Eng. Technol.* **2018**, *9*, 1485.
[52] "EN 316:2009 - Wood fibre boards - Definition, classification and symbols", iTeh Standards, https://standards.iteh.ai/catalog/standards/cen/4cc85e45-20ee-4daa-9ab9-2b85ad22b2b7/en-316-2009 (accessed: May 2024).
[53] D. Dai, M. Fan, in *Natural Fibre Composites*, (Eds:A. Hodzic, R. Shanks), Woodhead Publishing, Sawston, Cambridge, UK **2014**, pp. 3–65.
[54] J. Salimon, B. M. Abdullah, N. Salih, *Chem. Cent. J.* **2011**, *5*, 67.
[55] S. Bhakri, et al., *JRM* **2022**, *11*, 41.
[56] US EPA National Center for Environmental Assessment,"Optimization of Selective Epoxidation of Canola Oil with in situ Generated Peracetic Acid", https://hero.epa.gov/hero/index.cfm/reference/details/reference_id/4344157 (accessed: May 2023).

[57] Commissione tecnica per le industrie degli oli vegetali, grassi vegetali ed animali, delle proteine vegetali, degli oli minerali, dei colori e vernici, dei detergenti e tensioattivi, dei prodotti cosmetici e di igiene personale, *Norme italiane per il controllo dei grassi e derivati*, 3rd ed., (Milano: Stazione sperimentale per le industrie degli oli e dei grassi, **1976**), https://www.sciencedirect.com/science/article/pii/S1026309812001885.
[58] N. Tippayawong, P. Sittisun, *Scientia Iranica* **2012**, *19*, 1324.
[59] S. A. Roces, R. Tan, F. J. T. Da Cruz, S. C. Gong, R. K. Veracruz, *AJChE* **2011**, *11*, 41.
[60] L. G. Cançado, K. Takai, T. Enoki, M. Endo, Y. A. Kim, H. Mizusaki, A. Jorio, L. N. Coelho, R. Magalhães-Paniago, M. A. Pimenta, *Appl. Phys. Lett.* **2006**, *88*, 163106.
[61] H. Topsoe, *Bulletin* **1968**, *472*, 63.
[62] M. C. Menkiti, O. Ocheje, C. M. Agu, *Int J Ind Chem* **2017**, *8*, 133.
[63] C. A. Popoola, K. K. Ikpambese, *Icon Res Eng J* **2021**, *4*, 175.
[64] J. Ibarra, J. Melendres, M. Almada, M. G. Burboa, P. Taboada, J. Juárez, M. A. Valdez, *Mater. Res. Express* **2015**, *2*, 095010.
[65] N. S. Sayuti, R. Ali, S. T. Anuar, *UMT JUR* **2021**, *3*, 195.
[66] M. R. Plutino, C. Colleoni, I. Donelli, G. Freddi, E. Guido, O. Maschi, A. Mezzi, G. Rosace, *J. Colloid Interface Sci.* **2017**, *506*, 504.
[67] P. Launer, B. Arkles, in *Silicon Compounds: Silanes & Silicones*, (Eds: B. Arkles, G. L. Larson), Gelest Inc., Morrisville PA, **2013**, pp. 175–178.
[68] Z. Yuan, N. S. Kapu, D. M. Martinez, *Nord. Pulp Pap. Res. J.* **2017**, *32*, 4.
[69] B. Smith, *Spectroscopy* **2022**, *37*, 17.
[70] C. H. Dreimol, R. Kürsteiner, M. Ritter, A. Parrilli, J. Edberg, J. Garemark, S. Stucki, W. Yan, S. Tinello, G. Panzarasa, I. Burgert, *Small* **2024**, *20*, 2405558
[71] A. Dallinger, K. Keller, F. Greco, in *Nanoporous Carbons for Soft and Flexible Energy Devices*, (Eds: F. Borghi, F. Soavi, P. Milani), Springer International Publishing, Cham **2022**, pp. 111–133.
[72] A. C. Ferrari, D. M. Basko, *Nat. Nanotech* **2013**, *8*, 235.
[73] A. C. Ferrari, *Solid State Commun.* **2007**, *143*, 47.
[74] V. Kumar, A. Kumar, D.-J. Lee, S.-S. Park, *Materials* **2021**, *14*, 4590.
[75] C. K. de Carvalho Araújo, R. Salvador, C. Moro Piekarski, C. C. Sokulski, A. C. de Francisco, S. K. de Carvalho Araújo Camargo, *Sustainability* **2019**, *11*, 1057.